IEEE Transactions on Power Electronics

Data-Driven Modeling of Wireless Power Transfer Systems With Multiple Transmitters

Journal:	*IEEE Transactions on Power Electronics*
Manuscript ID	TPEL-Reg-2019-09-2151
Manuscript Type:	Regular Paper
Date Submitted by the Author:	26-Sep-2019
Complete List of Authors:	Chen, Fengwei; Wuhan University, School of Electrical Engineering and Automation Peter, Young; Lancaster University, Systems and Control Group Garnier, Hugues; Universite de Lorraine, CRAN Deng, Qijun; Wuhan University, School of Electrical Engineering and Automation Marian, Kazimierczuk; Wright State University
Keywords:	Parametric modeling, Identification, Resonant power conversion, Power electronics, Parameter estimation

Data-Driven Modeling of Wireless Power Transfer Systems With Multiple Transmitters

Fengwei Chen, Peter C. Young, Hugues Garnier, Qijun Deng, and Marian K. Kazimierczuk, *Fellow, IEEE*

***Abstract*—This paper develops a new method of data-driven modeling for a class of multiple-transmitter, single-receiver wireless power transfer (WPT) systems. A continuous-time, multiple-input, single-output (MISO) model with pure time delays is used to characterize the input–output behavior of the system, where the transfer functions associated with each input channel are not constrained to have the same denominator. Moreover, the time delays are allowed to be a fraction of the sample time in order to account for the delay effects that stem from circuit components and wireless communication which are, by nature, often a fraction of the sample time. An optimal instrumental variable method is proposed to estimate the parameters and time delays of the MISO model based on sampled input–output data. In contrast to the conventional circuit theory-based modeling methods that rely on circuit parameters and result in models which are often complex, the proposed data-driven method yields parsimonious models, whose parameters are directly estimated from input–output data. Due to the easy availability of input–output data in control engineering applications, the proposed method is clearly more user-friendly, having a broad prospect for efficient operation of WPT systems, such as prediction, optimization, and control. Numerical and experimental results are presented to validate the effectiveness and merit of the proposed method.**

***Index Terms*—Data-driven modeling, instrumental variable method, multiple-input single-output (MISO) system, time-delay estimation, wireless power transfer (WPT).**

I. Introduction

WIRELESS power transfer (WPT) based on magnetic resonant coupling has been recognized as a preferred technology for mid-range power delivery [1], [2]. WPT is beneficial for scenarios, where power cable connections are inconvenient or not allowed, with applications ranging from portable devices [3], wireless sensors [4], biomedical implants [5], [6], to electric vehicles [7]–[9]. The power transfer efficiency of WPT systems is known to be very sensitive to the coupling link between the transmitter and receiver coils, while magnetic coupling is strongly dependent on factors such as coil geometry, coil placement and ambient interference. In view of this background, there are a few papers where multiple or arrayed transmitters are employed to power a single receiver in order to improve the range, reliability and gain of power transfer. These show that multiple-input, single-output (MISO) WPT systems generally outperform their single-input, single-output (SISO) counterparts in terms of overall power transfer efficiency [10]–[15]. At the same time, however, use of multiple transmitters brings new challenges for analysis, design, and optimization of WPT systems, due to the increase in the number of degrees of freedom [13].

Over the last few years, considerable efforts have been made to address the above-mentioned problems. In [10], an upper bound of power transfer efficiency in the near-field WPT under the multiple-transmitter scenario was established. In [11], the effect of coupling between transmitters and receivers was investigated and some guidelines were suggested on how to adjust the resonant and/or driving frequencies for maximum efficiency. In [12], the coupling, gain, and diversity effects were investigated in further detail with the help of a simple circuit model and a new power line synchronization technique was proposed to synchronize all transmitter coils to achieve maximum efficiency. More recently, a new convex optimization framework was formulated in [13] to optimize the power transfer efficiency, where the original non-convex problem was reformulated into a convex one, so that constraints on the transmitting power could be imposed conveniently.

The aforementioned papers all concentrated on circuit-level analysis of MISO WPT systems, while system-level analysis, with particular reference to dynamic modeling in the input–output form necessary for control design, has been considered less. To fill this gap, the focus of this paper is on the control-oriented modeling of MISO WPT systems. There are already several circuit theory-based methods available in the literature [16]–[23], and a few of them can build transfer function or state-space models for SISO WPT systems, e.g., the first-harmonic approximation method [17], [18]; the state-space averaging method [19]; the coupled mode-based method [20]; and the sampled-data model approach [22]. The above-mentioned methods have been shown to be effective when the circuit component parameters are known *a priori* or can be experimentally measured. However, the determination of these parameters is often difficult in industrial applications

This paper was supported in part by the National Natural Science Foundation of China under Grants 61703311, 51677139, 51977151, and 61903057, in part by the China Postdoctoral Science Foundation under Grant 2017M620335, and in part by the Shenzhen Science and Technology Innovation Committee under Grant JCYJ2017081811280674.

F. Chen is with the School of Electrical Engineering and Automation, Wuhan University, Wuhan 430072, China (e-mail: fengwei.chen@whu.edu.cn).

P. C. Young is with the Systems and Control Group, Lancaster Environment Centre, Lancaster University, Lancaster LA1 4YQ, UK (e-mail: p.young@lancaster.ac.uk).

H. Garnier is with the Centre de Recherche en Automatique de Nancy, Centre National de la Recherche Scientifique, Université de Lorraine, F-54000 Nancy, France (e-mail: hugues.garnier@univ-lorraine.fr).

Q. Deng is with the School of Electrical Engineering and Automation, Wuhan University, Wuhan 430072, China, and also with the Shenzhen Research Institute, Wuhan University, Shenzhen 518057, China (e-mail: dqj@whu.edu.cn).

M. K. Kazimierczuk is with the Department of Electrical Engineering, Wright State University, Dayton, OH 45435, USA (e-mail: marian.kazimierczuk@wright.edu).

due to technical or economic reasons and, consequently, good performance of conventional methods may not be guaranteed, especially when the system parameters can vary with respect to time. In addition, these methods were initially developed for SISO WPT systems, so that their generalization to the MISO scenario is not trivial because coupling also occurs among the transmitters, not only between the transmitters and receiver, making the circuit analysis very difficult. Another shortcoming of circuit theory-based methods is the complication of the resulting models, which are of high order and not suitable for control system design unless a model reduction step has been performed [24], [25]. In this regard, it is necessary to develop an efficient and user-friendly method for fast and accurate dynamic modeling.

In contrast to circuit theory-based modeling, data-driven modeling, referred to as 'system identification' in the control literature [26]–[28], adopts a rather straightforward approach to avoid the problem of over-parameterization. In particular, it uses a parsimonious, gray- or black-box model, the order and structure of which is identified from the data, to fit the output data; and then estimates the parameters that characterize this model by minimizing a quadratic cost function defined by the mean-squared errors between the predicted and measured outputs [27]. Since sampled input–output data are easier to acquire than the true circuit component parameters, the data-driven approach is more user-friendly and can always yield simple models that are very suitable for control system design. Therefore, data-driven modeling has been attracting increasing attention in the field of power electronics [29]–[32]. Moreover, as the model parameters are optimal in the mean-squared error sense and no model reduction is necessary, the data-driven approach can outperform the conventional approaches in terms of model efficiency and accuracy.

In our previous work [25], data-driven modeling of a SISO WPT system has been investigated, using a continuous-time (CT) or discrete-time (DT) transfer function, plus a time delay, to explain the input–output behavior of the system. Here, the method employed to estimate the associated model parameters and time delay is the frequency-domain version of the instrumental variable (IV)-based method proposed in [33]. The merit of modeling in the frequency-domain is that both CT and DT models can be estimated in a uniform manner. In this paper, we generalize the method in [33] to estimate MISO time-delay models for WPT systems. The contributions of this paper are twofold:

- A parsimonious MISO model with pure time delays is proposed to explain the input–output behavior of a MISO WPT system, where *parsimonious* means that the number of parameters is as small as necessary to explain the input–output behavior of the system. Here, for parsimonious parameterization, the transfer functions associated with each transmitter are not constrained to have the same denominator, so allowing for fully independent parameterization of each transmitter channel.
- Robust implementation of the proposed method is investigated. The generalization of the method in [33] to estimate MISO time-delay models is more challenging than in the SISO case, due to the multi-modality nature of the cost function, which becomes more severe in the presence of multiple time delays. Therefore, how to increase the chance of global convergence is a problem of great practical value.

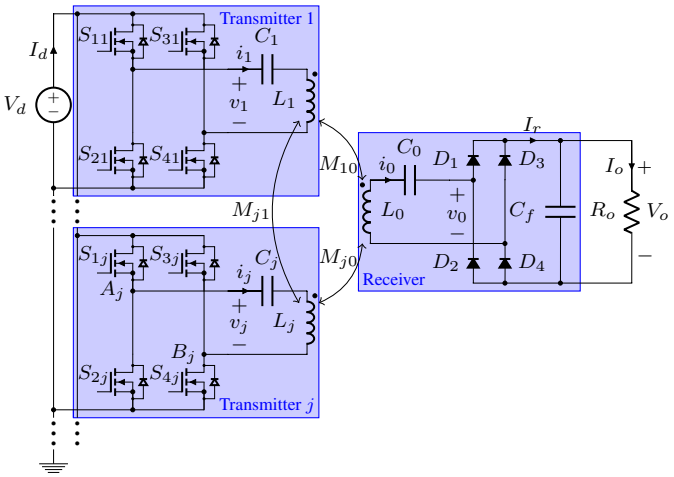

Fig. 1. MISO WPT system under consideration.

The remainder of this paper is organized as follows. The MISO WPT system and its model are introduced in Section II. After that, a new refined IV (RIV)-based method to estimate the parameters and time delays of the model is proposed in Section III. Practical considerations for efficient implementation of the proposed method are discussed in Section IV. Subsequently, simulation and experimental examples are presented in Sections V and VI to confirm the merit and effectiveness of the proposed method. Finally, conclusions are drawn in Section VII.

II. Preliminaries

A. WPT System

This paper considers a series–series compensated MISO WPT system, as shown diagrammatically in Fig. 1. Each transmitter consists of a phase-controlled full-bridge inverter S_{1j}–S_{4j}, a coil L_j, and a compensating capacitor C_j, $1 \leqslant j \leqslant n_u$, where n_u is the number of transmitters. The receiver consists of a coil L_0, a compensating capacitor C_0, a full-bridge rectifier D_1–D_4, and an output filter capacitor C_f. This WPT setup assumes loose coupling between the transmitter and receiver coils; i.e., the mutual inductance $M_{jk}, 0 \leqslant j \leqslant n_u, 0 \leqslant k \leqslant n_u, j \neq k$, is small, while the leakage inductance is large, so that the role of C_j is to compensate for the inductive behavior of L_j; see [21], [34] for more analysis and design issues regarding loosely coupled transformers. The merit of series–series compensation is that the choice of the compensating capacitors is independent of the load [18]. In order to allow for significant power transfer through loosely coupled coils, however, the transmitter and receiver resonators should have the same resonant frequency defined by [35]

$$f_0 = \frac{1}{2\pi\sqrt{L_0 C_0}} = \cdots = \frac{1}{2\pi\sqrt{L_{n_u} C_{n_u}}} \text{ Hz} \qquad (1)$$

and the driving frequencies of each inverter need to be synchronized with the same frequency f_0 and phase [12].

For regulation of the output voltage V_o, a set of control variables, denoted as $\{\alpha_j\}$, are often chosen as the phase between the leading leg (S_{1j} and S_{2j}) and the lagging leg (S_{3j} and S_{4j}); see also [36]–[38]. When α_j varies from 0 to 180°, V_o reduces from the maximum to the minimum. Furthermore, conventional circuit theory-based methods can be used to obtain a model that relates the inputs $\{\alpha_j\}$ and the output V_o necessary for control design.

The remainder of this subsection recalls briefly some of the shortcomings of circuit theory-based methods and proposes a data-driven approach that is free from these problems. Due to the fact that the AC source v_j is not an explicit function of α_j, conventional methods cannot yield a model directly in an input–output form. Consequently, one needs to approximate v_j as follows, by its first harmonic [25]:

$$\begin{aligned} v_j &= v_{a,j} - v_{b,j} \\ &\approx \frac{2V_d}{\pi}\left[\sin\left(\omega_s t + \frac{\alpha_j}{2}\right) - \sin\left(\omega_s t - \pi - \frac{\alpha_j}{2}\right)\right] \\ &= \frac{4V_d}{\pi}\cos\left(\frac{\alpha_j}{2}\right) \times \sin(\omega_s t) \end{aligned} \tag{2}$$

where $v_{a,j}$ and $v_{b,j}$ denote the voltages at points A_j and B_j, respectively, in Fig. 1. As can be seen from (2), α_j is now explicit in v_j, but they are still nonlinearly related, so an additional linearization step is required. Let $z_j = \overline{z}_j + \tilde{z}_j$, where $z = v$ or α, and $\overline{z}$ and $\tilde{z}$ denote the static and small-signal parts of z, respectively. Then, v_j can be linearized around $\overline{v}_j$ by first-order Taylor expansion, i.e.,

$$\tilde{v}_j \approx -\frac{2V_d}{\pi}\sin\left(\frac{\overline{\alpha}_j}{2}\right)\tilde{\alpha}_j \times \sin(\omega_s t). \tag{3}$$

Subsequently, repeating the same procedure to the other signals in the circuit and applying the dq decomposition to eliminate the $\sin(\omega_s t)$ and $\cos(\omega_s t)$ terms (see also [17]), a linear small-signal model that relates $\{\tilde{\alpha}_j\}$ and $\tilde{v}_o$ can be obtained by using Kirchoff's laws. Since modeling methods of this kind have been well-known in the literature, they will not be reproduced here, but the interested reader is directed to papers such as [18], [25] for further details. Clearly, the requirement of true circuit component parameters, harmonic approximation, and linearization mean that the modeling methods are not easy to use. In the next subsection, a data-driven method is proposed that avoids these difficulties.

B. Model Formulation

For clarity of notations, the input $\tilde{\alpha}_j$ and output $\tilde{v}_o$ defined in the previous subsection are written, hereafter as $u_j(t)$ and $y(t)$, respectively. The following hybrid Box–Jenkins (HBJ) model [39], [40] with n_u inputs is used to describe the input–output behavior of the system (see also Fig. 2):

$$\begin{cases} x_j(t) = G(p,\boldsymbol{\theta}_j)u(t-\tau_j) = \dfrac{B(p,\boldsymbol{\theta}_j)}{A(p,\boldsymbol{\theta}_j)}u_j(t-\tau_j) \\ \xi(t_k) = H(q^{-1},\boldsymbol{\eta})e(t_k) = \dfrac{D(q^{-1},\boldsymbol{\eta})}{C(q^{-1},\boldsymbol{\eta})}e(t_k) \\ y(t_k) = \sum_{j=1}^{n_u} x_j(t_k) + \xi(t_k) \end{cases} \tag{4}$$

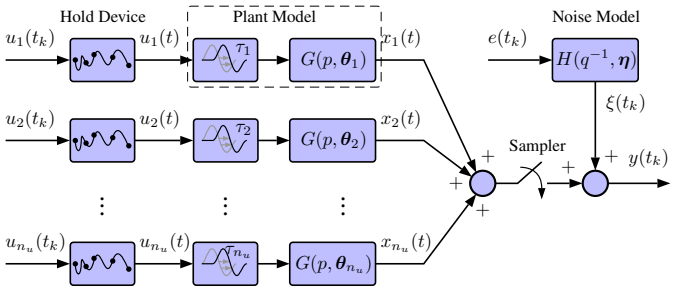

Fig. 2. Block diagram of the HBJ model with n_u inputs given in (4).

where $t_k = kT$ is the sampling instant with T denoting the sample time. Note that a noise model is included in (4) to improve the explanatory ability of the whole model, as colored noise is commonly encountered in real applications, or can be artificially introduced during the measurement process, e.g., using an LCR low-pass filter to avoid the aliasing effect.

The word *hybrid* means that the plant is modeled in the CT domain, while the noise is modeled in the DT domain. This hybrid formulation of the model is motivated by the difficulty in estimating a CT noise model directly in a stochastic differential equation form when the alternative DT noise model is entirely adequate in stochastic terms and much simpler to estimate. CT models of the main system dynamics are appealing in several aspects [41]–[44]. Firstly, CT model parameters may provide physical insights into the system and, thus, are particularly suitable for physical modeling. Secondly, when the sample time is too small, DT models suffer from the problem of numerical instability, but CT models do not have this problem since CT model parameters are independent of the sample time. Thirdly, CT models are a natural choice to handle fractional time delays while, in DT models, time delays are always constrained to be an integer number of sampling intervals, due to the use of shift operators.

$G(p,\boldsymbol{\theta}_j)$ is the rational transfer function of the jth transmitter channel, whose numerator and denominator polynomials are of the forms

$$B(p,\boldsymbol{\theta}_j) = b_{0,j}p^{m_j} + b_{1,j}p^{m_j-1} + \cdots + b_{m_j,j} \tag{5}$$

$$A(p,\boldsymbol{\theta}_j) = p^{n_j} + a_{1,j}p^{n_j-1} + \cdots + a_{n_j,j} \tag{6}$$

where p is the differentiation operator: $px_j(t) = dx_j(t)/dt$, n_j and m_j ($n_j \geqslant m_j$) are polynomial degrees, and $\boldsymbol{\theta}_j$ is a vector of the unknown rational model parameters

$$\boldsymbol{\theta}_j = \left[a_{1,j},\ldots,a_{n_j,j},b_{1,j},\ldots,b_{m_j,j}\right]^\top. \tag{7}$$

The colored noise $\xi(t_k)$ is modeled as a filtered version of white noise $e(t_k)$, which is unmeasurable, through a DT auto-regressive moving average (ARMA) model $H(q^{-1},\boldsymbol{\eta})$, the polynomials of which are defined in terms of the shift operator q^{-1}, i.e., $q^{-1}\xi(t_k) = \xi(t_{k-1})$, as

$$D(q^{-1},\boldsymbol{\eta}) = 1 + d_1q^{-1} + \cdots + d_{n_d} \tag{8}$$

$$C(q^{-1},\boldsymbol{\eta}) = 1 + c_1q^{-1} + \cdots + c_{n_c} \tag{9}$$

and the unknown model parameters are gathered in vector $\boldsymbol{\eta}$

$$\boldsymbol{\eta} = [c_1, \ldots, c_{n_c}, d_1, \ldots, d_{n_d}]^\top . \tag{10}$$

C. Objective

Assume that the following conditions are considered as satisfied throughout this paper:

1) The CT input $u_j(t)$ is generated from a DT sequence $\{u_j(t_k)\}_{k=1}^N$ via a known hold device. $\{u_j(t_k)\}_{j=1}^{n_u}$ are zero mean, mutually uncorrelated, and persistently exciting.
2) $G(p, \boldsymbol{\theta}_j)$ is compact, causal, and asymptotically stable. More specifically, the roots of $A(p, \boldsymbol{\theta}_j)$ are all located on the left-half plane; $B(p, \boldsymbol{\theta}_j)$ and $A(p, \boldsymbol{\theta}_j)$ do not have any common factors. Moreover, the denominators $\{A(p, \boldsymbol{\theta}_j)\}_{j=1}^{n_u}$ are not necessarily constrained to be identical.
3) $H(q^{-1}, \boldsymbol{\eta})$ is stable and invertible, that is, $C(q^{-1}, \boldsymbol{\eta})$ and $D(q^{-1}, \boldsymbol{\eta})$ are co-prime, with all roots located within the unit circle. $e(t_k)$ is zero mean, white, and uncorrelated with the inputs.
4) The degrees $\{n_j, m_j\}_{j=1}^{n_u}$, n_c, and n_d are known.

The objective of this paper is to estimate the parameter vectors $\{\boldsymbol{\theta}_j\}_{j=1}^{n_u}$ and $\boldsymbol{\eta}$, and the time delays $\{\tau_j\}_{j=1}^{n_u}$ from the sampled input–output data $\{y(t_k), u_1(t_k), \ldots, u_{n_u}(t_k)\}_{k=1}^N$.

III. Proposed Methodology

In this section, a new method is proposed to estimate MISO time-delay models for MISO WPT systems based on the method developed in our previous paper [45]. To handle the scenario that the denominators associated with each input are not identical, an iterative, multi-linear regression technique [45], [46] is adopted. Before going further, let us first define the prediction error cost function as follows:

$$J(\boldsymbol{\vartheta}) = \frac{1}{N}\sum_{k=1}^{N} \|\varepsilon(t_k, \boldsymbol{\vartheta})\|_2^2 \tag{11}$$

$$\varepsilon(t_k, \boldsymbol{\vartheta}) = \frac{1}{H(q^{-1}, \boldsymbol{\eta})}\left[y(t_k) - \sum_{j=1}^{n_u} G(p, \boldsymbol{\theta}_j) u_j(t_k - \tau_j)\right] \tag{12}$$

where $\boldsymbol{\vartheta} = \left[\boldsymbol{\theta}_1^\top, \tau_1, \ldots, \boldsymbol{\theta}_{n_u}^\top, \tau_{n_u}, \boldsymbol{\eta}^\top\right]^\top$ is a vector of the whole unknown parameters, and the optimization problem

$$\hat{\boldsymbol{\vartheta}} = \arg\min_{\boldsymbol{\vartheta}} J(\boldsymbol{\vartheta}). \tag{13}$$

Since the dimensionality of $\boldsymbol{\vartheta}$ can be high in the MISO setting, the optimization problem (13) will be solved in a separable fashion to avoid the problem of ill-conditioning, with the parameters associated with each plant model and the noise model being estimated separately. This strategy is benefited from the first and third conditions of Section II-C, which ensure a block-diagonal error covariance matrix of $\boldsymbol{\vartheta}$, i.e.,

$$P_{\boldsymbol{\vartheta}} = \begin{bmatrix} P_1 & & 0 \\ & \ddots & \\ 0 & & P_{n_u+1} \end{bmatrix} \tag{14}$$

each block P_j corresponding to the error covariance matrix of the pair $\{\boldsymbol{\theta}_j, \tau_j\}$ if $1 \leqslant j \leqslant n_u$, or $\boldsymbol{\eta}$ if $j = n_u + 1$. The above property allows us to estimate the parameters of each block separately.

A. Plant Model Parameter Estimation

The method of plant model estimation is based on the idea of decomposing a MISO model into n_u SISO models. Assuming that the output of the jth model is $y_j(t_k)$, and that $\boldsymbol{\eta}$ is known tentatively, the prediction error $\varepsilon(t_k, \boldsymbol{\vartheta})$ can be formulated in the following multi-linear regression form [45]:

$$\begin{aligned}\varepsilon(t_k, \boldsymbol{\vartheta}) &= \sum_{j=1}^{n_u} \frac{1}{H(q^{-1}, \boldsymbol{\eta})}\left[y_j(t_k) - G(p, \boldsymbol{\theta}_j) u_j(t_k - \tau_j)\right] \\ &= \sum_{j=1}^{n_u} \frac{1}{A(p, \boldsymbol{\theta}_j) H(q^{-1}, \boldsymbol{\eta})}[A(p, \boldsymbol{\theta}_j) y_j(t_k) \\ &\quad - B(p, \boldsymbol{\theta}_j) u_j(t_k - \tau_j)] \\ &= \sum_{j=1}^{n_u} \tilde{y}_j^{(n_j)}(t_k) - \tilde{\boldsymbol{\phi}}_j^\top(t_k, \tau_j)\boldsymbol{\theta}_j \end{aligned} \tag{15}$$

where the filtered regression vectors are of the form

$$\begin{aligned}\tilde{\boldsymbol{\phi}}_j^\top(t_k, \tau_j) = \Big[&- \tilde{y}_j{}^{(n_j-1)}(t_k), \ldots, -\tilde{y}_j(t_k), \\ &\tilde{u}_j^{(m_j)}(t_k - \tau_j), \ldots, \tilde{u}_j(t_k - \tau_j)\Big] \end{aligned} \tag{16}$$

in which $\tilde{z}_j(t_k)$, $z = y$ or u, stands for the filtered version of $z_j(t_k)$ using the hybrid filter $1/A(p, \boldsymbol{\theta}_j) \cdot 1/H(q^{-1}, \boldsymbol{\eta})$.

It is interesting to observe from (15) that the estimation of $\{\boldsymbol{\theta}_j\}_{j=1}^{n_u}$ can be facilitated by solving a set of n_u linear regression problems, each being simpler than the original problem. Unfortunately, this idea cannot be directly implemented, due to the requirement of $y_j(t_k)$, which is unmeasured (only $y(t_k)$ is measured), and $\boldsymbol{\theta}_j$, which is unknown *a priori*. This problem can be avoided by using a bootstrap procedure for implementation: namely, by constructing the filters and auxiliary models based on initial values $\boldsymbol{\theta}_j^*$ and τ_j^*, we have

$$\tilde{z}_j^{(i)}(t_k) = \frac{p^i}{A(p, \boldsymbol{\theta}_j^*)} \cdot \frac{1}{H(q^{-1}, \boldsymbol{\eta})} z_j(t_k), \ z = y \text{ or } u \tag{17}$$

$$y_j(t_k) = y(t_k) - \sum_{i=1, i\neq j}^{n_u} G(p, \boldsymbol{\theta}_i^*) u_i(t_k - \tau_i^*). \tag{18}$$

Filtering a signal in the CT domain using DT data requires knowledge of the inter-sample behavior: see [47] for more details on the digital implementation.

Based on the data set $\{y_j(t_k), u_j(t_k)\}_{k=1}^N$, the vector of rational parameters of the jth SISO model $\boldsymbol{\theta}_j$ can be sequentially estimated by repeatedly applying an existing SISO modeling method with τ_j being fixed. An IV method of estimation is normally used, as in the present paper, because least-squares estimation generates biased estimates in the presence of measurement noise (due to the correlation between the regression vector and the measurement noise).

Without loss of generality, based on (15) and following [40], the IV estimates of the parameters and the time delay of each

SISO model are defined to solve the following problem:

$$\begin{bmatrix}\hat{\boldsymbol{\theta}}_j\\ \hat{\tau}_j\end{bmatrix} = \arg\min_{\boldsymbol{\theta}_j,\tau_j} \sum_{k=1}^{N} \begin{bmatrix}\hat{\boldsymbol{\phi}}_j(t_k)\\ \hat{\boldsymbol{\psi}}_j(t_k)\end{bmatrix} \left[\tilde{y}_j^{(n_j)}(t_k) - \tilde{\boldsymbol{\phi}}_j^{\top}(t_k,\tau_j)\boldsymbol{\theta}_j\right] \tag{19}$$

where $\hat{\boldsymbol{\phi}}_j(t_k)$ and $\hat{\boldsymbol{\psi}}_j(t_k)$ are the instruments used in the estimation of $\boldsymbol{\theta}_j$ and τ_j, respectively. The problem (19) is also solved in a separable fashion according to [33], and further details are given in the next two subsections.

1) Rational Model Parameter Estimation: When τ_j is assumed to be fixed tentatively, an IV estimate of $\boldsymbol{\theta}_j$ as a function of τ_j is readily computed as

$$\hat{\boldsymbol{\theta}}_j(\tau_j) = \left[\sum_{k=1}^{N} \hat{\boldsymbol{\phi}}_j(t_k)\tilde{\boldsymbol{\phi}}_j^{\top}(t_k,\tau_j)\right]^{-1} \sum_{k=1}^{N} \hat{\boldsymbol{\phi}}_j(t_k)\tilde{y}_j^{(n_j)}(t_k). \tag{20}$$

According to the criterion that the instrument should be maximally correlated with the regression vector but uncorrelated with the noise, the RIV method, which is one of the most successful implementation of the IV techniques, uses the following instrument [28]:

$$\begin{aligned}\hat{\boldsymbol{\phi}}_j^{\top}(t_k) = \Big[&-\hat{x}_j^{(n_j-1)}(t_k),\ldots,-\hat{x}_j(t_k),\\ &\tilde{u}_j^{(m_j)}(t_k-\tau_j^*),\ldots,\tilde{u}_j(t_k-\tau_j^*)\Big]\end{aligned} \tag{21}$$

where $\hat{x}_j(t_k)$ is the noise-free version of $\tilde{y}_j(t_k)$ generated by the following auxiliary model parameterized by $\boldsymbol{\theta}_j^*$ and τ_j^*:

$$\hat{x}_j(t_k) = G(p,\boldsymbol{\theta}_j^*)\tilde{u}_j(t_k-\tau_j^*). \tag{22}$$

2) Time Delay Estimation: By substituting (20) into (19), the optimization problem reduces to

$$\hat{\tau}_j = \arg\min_{\tau_j} \sum_{k=1}^{N} \hat{\boldsymbol{\psi}}_j(t_k)\left[\tilde{y}_j^{(n_j)}(t_k) - \tilde{\boldsymbol{\phi}}_j^{\top}(t_k,\tau_j)\hat{\boldsymbol{\theta}}_j(\tau_j)\right]. \tag{23}$$

As τ_j is nonlinear in the above expression, a gradient-based searching procedure can be employed for optimization

$$\hat{\tau}_j = \tau_j^* - \mu\left[\nabla^2\breve{J}(\tau_j^*)\right]^{-1}\nabla\breve{J}(\tau_j^*) \tag{24}$$

where μ is a scaling factor that defines the step length; $\nabla\breve{J}(\tau_j)$ and $\nabla^2\breve{J}(\tau_j)$ are the gradient and Hessian, respectively, which can be approximated as

$$\nabla\breve{J}(\tau_j) = -\sum_{k=1}^{N}\hat{\boldsymbol{\psi}}_j(t_k)\breve{\varepsilon}_j(t_k,\tau_j) \tag{25}$$

$$\nabla^2\breve{J}(\tau_j) = -\sum_{k=1}^{N}\hat{\boldsymbol{\psi}}_j(t_k)\frac{\partial\breve{\varepsilon}_j(t_k,\tau_j)}{\partial\tau_j} \tag{26}$$

where $\breve{\varepsilon}_j(t_k,\tau_j) = \tilde{y}_j^{(n_j)}(t_k) - \tilde{\boldsymbol{\phi}}_j^{\top}(t_k,\tau_j)\hat{\boldsymbol{\theta}}_j(\tau_j)$. Following (15) and (20), $-\partial\breve{\varepsilon}_j(t_k,\tau_j)/\partial\tau_j$ involved in the above equation is computed as

$$\begin{aligned}-\frac{\partial\breve{\varepsilon}_j(t_k,\tau_j)}{\partial\tau_j} &= \frac{\partial\tilde{\boldsymbol{\phi}}_j^{\top}(t_k,\tau_j)}{\partial\tau_j}\hat{\boldsymbol{\theta}}_j(\tau_j) + \tilde{\boldsymbol{\phi}}_j^{\top}(t_k,\tau_j)\frac{d\hat{\boldsymbol{\theta}}_j(\tau_j)}{d\tau_j}\\ &= \frac{\partial\tilde{\boldsymbol{\phi}}_j^{\top}(t_k,\tau_j)}{\partial\tau_j}\hat{\boldsymbol{\theta}}_j(\tau_j) - \tilde{\boldsymbol{\phi}}_j^{\top}(t_k,\tau_j)\\ &\quad\times\left[\sum_{k=1}^{N}\hat{\boldsymbol{\phi}}_j(t_k)\tilde{\boldsymbol{\phi}}_j^{\top}(t_k,\tau_j)\right]^{-1}\\ &\quad\times\sum_{k=1}^{N}\hat{\boldsymbol{\phi}}_j(t_k)\frac{\partial\tilde{\boldsymbol{\phi}}_j^{\top}(t_k,\tau_j)}{\partial\tau_j}\hat{\boldsymbol{\theta}}_j(\tau_j).\end{aligned} \tag{27}$$

Letting $\boldsymbol{\psi}_j^{\top}(t_k,\tau_j) = \left[\partial\tilde{\boldsymbol{\phi}}_j^{\top}(t_k,\tau_j)/\partial\tau_j\right]\hat{\boldsymbol{\theta}}_j(\tau_j)$, we have

$$\begin{aligned}\nabla^2\breve{J}(\tau_j) = &\sum_{k=1}^{N}\hat{\boldsymbol{\psi}}_j(t_k)\boldsymbol{\psi}_j^{\top}(t_k,\tau_j) - \sum_{k=1}^{N}\hat{\boldsymbol{\psi}}_j(t_k)\tilde{\boldsymbol{\phi}}_j^{\top}(t_k,\tau_j)\\ &\times\left[\sum_{k=1}^{N}\hat{\boldsymbol{\phi}}_j(t_k)\tilde{\boldsymbol{\phi}}_j^{\top}(t_k,\tau_j)\right]^{-1}\\ &\times\sum_{k=1}^{N}\hat{\boldsymbol{\phi}}_j(t_k)\boldsymbol{\psi}_j^{\top}(t_k,\tau_j).\end{aligned} \tag{28}$$

The last question that remains to be answered is how to choose the instrument $\hat{\boldsymbol{\psi}}_j(t_k)$. Motivated by (21) that $\hat{\boldsymbol{\phi}}_j^{\top}(t_k)$ is, in fact, the noise-free version of the partial derivative of $-\varepsilon(t_k,\boldsymbol{\vartheta})$ with respect to $\boldsymbol{\theta}_j$ evaluated at $\boldsymbol{\theta}_j^*$ and τ_j^*, $\hat{\boldsymbol{\psi}}_j(t_k)$ can be chosen along the same line, namely

$$\begin{aligned}&\hat{\boldsymbol{\psi}}_j(t_k)\\ &= -\frac{\partial\varepsilon(t_k,\boldsymbol{\vartheta})}{\partial\tau_j}\bigg|_{\boldsymbol{\theta}_j=\boldsymbol{\theta}_j^*,\tau_j=\tau_j^*}\\ &= \frac{\partial\tilde{\boldsymbol{\phi}}_j^{\top}(t_k,\tau_j)}{\partial\tau_j}\boldsymbol{\theta}_j^*\bigg|_{\tau_j=\tau_j^*}\\ &= -\left[0,\ldots,0,\tilde{u}_j^{(m_j+1)}(t_k-\tau_j^*),\ldots,\tilde{u}_j^{(1)}(t_k-\tau_j^*)\right]\boldsymbol{\theta}_j^*\\ &= -\left[pG(p,\boldsymbol{\theta}_j^*)/H(q^{-1},\boldsymbol{\eta})\right]u_j(t_k-\tau_j^*)\end{aligned} \tag{29}$$

where the relation $\partial\tilde{u}_j(t-\tau_j)/\partial\tau_j = -\partial u_j(t-\tau_j)/\partial t$ has been used in deriving the third equality of the above equation.

Finally, on convergence, the estimation error covariance matrix can be computed according to [40] as follows:

$$P_{\boldsymbol{\theta}_j} = \sigma_\varepsilon^2\left[\sum_{k=1}^{N}\hat{\boldsymbol{\phi}}_j(t_k)\hat{\boldsymbol{\phi}}_j^{\top}(t_k)\right]^{-1} \tag{30}$$

$$\begin{aligned}P_{\tau_j} = \sigma_\varepsilon^2\Bigg\{&\sum_{k=1}^{N}\hat{\boldsymbol{\psi}}_j(t_k)\hat{\boldsymbol{\psi}}_j^{\top}(t_k) - \sum_{k=1}^{N}\hat{\boldsymbol{\psi}}_j(t_k)\hat{\boldsymbol{\phi}}_j^{\top}(t_k)\\ &\times\left[\sum_{k=1}^{N}\hat{\boldsymbol{\phi}}_j(t_k)\hat{\boldsymbol{\phi}}_j^{\top}(t_k)\right]^{-1}\sum_{k=1}^{N}\hat{\boldsymbol{\phi}}_j(t_k)\hat{\boldsymbol{\psi}}_j^{\top}(t_k)\Bigg\}^{-1}\end{aligned} \tag{31}$$

where σ_ε^2 is the variance of the prediction error.

B. Noise Model Parameter Estimation

When the plant model parameters have been obtained, the colored measurement noise can be estimated as

$$\hat{\xi}(t_k) = y(t_k) - \sum_{j=1}^{n_u} G(p,\hat{\boldsymbol{\theta}}_j)u_i(t_k-\hat{\tau}_j) \tag{32}$$

Algorithm 1: The basic TFRIVC method.

Input:
- Sampled data: $\{y(t_k), u_1(t_k), \ldots, u_{n_u}(t_k)\}_{k=1}^{N}$;
- Polynomial degrees: $\{n_j, m_j\}_{j=1}^{n_u}$, n_c, n_d;
- Initial parameter vector: $\boldsymbol{\vartheta}^*$;
- Maximum iteration number: $N_{\max}$;
- Tolerances of cost and parameter changes: ς_{fun}, ς_{par};
- Lower and upper time-delay boundaries: $\{\underline{\tau}_j, \overline{\tau}_j\}_{j=1}^{n_u}$;

Output: $\boldsymbol{\vartheta}^*$;

for $r \leftarrow 1$ **to** $N_{\max}$ **do**
  $\mu \leftarrow 1$;
  for $j \leftarrow 1$ **to** n_u **do**
    compute $y_j(t_k)$ in (18), $\nabla J(\tau_j^*)$ in (25), and $\nabla^2 J(\tau_j^*)$ in (26) using $\boldsymbol{\vartheta}^*$;
    compute the time-delay increment
    $$\Delta\tau_j \leftarrow \left[\nabla^2 \breve{J}(\tau_j^*)\right]^{-1} \nabla \breve{J}(\tau_j^*);$$
    while $\tau_j^* - \mu\Delta\tau_j \notin [\underline{\tau}_j, \overline{\tau}_j]$ **do** $\mu \leftarrow \mu/2$;
  end
  for $i \leftarrow 1$ **to** $N_{\max}$ **do**
    for $j \leftarrow 1$ **to** n_u **do**
      update the time delay: $\hat{\tau}_j \leftarrow \tau_j^* - \mu\Delta\tau_j$;
      compute $\tilde{\boldsymbol{\phi}}_j^\top(t_k, \hat{\tau}_j)$ in (16), $\tilde{y}_j^{(n_j)}(t_k)$ in (17), and $\hat{\boldsymbol{\phi}}_j^\top(t_k)$ in (21) using $\boldsymbol{\theta}_j^*$ and $\hat{\tau}_j$;
      generate $\hat{\boldsymbol{\theta}}_j$ using the IV estimator
      $$\hat{\boldsymbol{\theta}}_j \leftarrow \left[\sum_{k=1}^{N} \hat{\boldsymbol{\phi}}_j(t_k)\tilde{\boldsymbol{\phi}}_j^\top(t_k, \hat{\tau}_j)\right]^{-1} \times \sum_{k=1}^{N} \hat{\boldsymbol{\phi}}_j(t_k)\tilde{y}_j^{(n_j)}(t_k);$$
    end
    compute $\hat{\xi}(t_k)$ in (32) using $\{\hat{\boldsymbol{\theta}}_j, \hat{\tau}_j\}_{j=1}^{n_u}$ and, based on which, generate $\hat{\boldsymbol{\eta}}$ using an ARMA estimation routine;
    compute the cost $J(\hat{\boldsymbol{\vartheta}})$ in (11);
    if $J(\hat{\boldsymbol{\vartheta}}) \geqslant J(\boldsymbol{\vartheta}^*)$ **then**
      $\mu \leftarrow \mu/2$;
      if $\|\Delta\boldsymbol{\vartheta}^*./\boldsymbol{\vartheta}^*\| < \varsigma_{\text{par}}$ **then** break;
    else
      $\boldsymbol{\vartheta}^* \leftarrow \hat{\boldsymbol{\vartheta}}$;
      break;
    end
  end
  if $|\Delta J(\boldsymbol{\vartheta}^*)/J(\boldsymbol{\vartheta}^*)| < \varsigma_{\text{fun}}$ or $\|\Delta\boldsymbol{\vartheta}^*./\boldsymbol{\vartheta}^*\| < \varsigma_{\text{par}}$ **then** break;
end

and then, based on the estimated sequence $\{\hat{\xi}(t_k)\}_{k=1}^{N}$, standard routines can be used to estimate the vector of ARMA model parameters $\boldsymbol{\eta}$, such as that used in [40].

C. The Complete Algorithm

The complete algorithm of the proposed method, referred to as Refined Instrumental Variable for Continuous-time Transfer Function (TFRIVC[1]) models, is summarized in Algorithm 1.

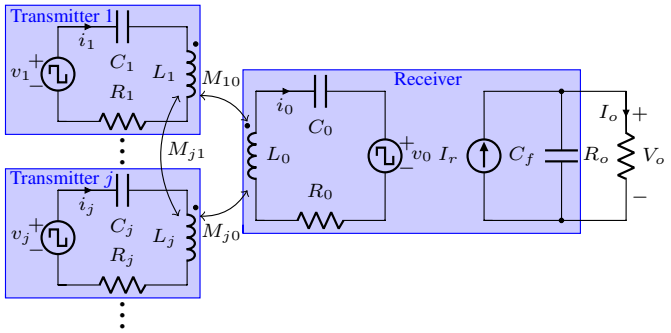

Fig. 3. Equivalent circuit of Fig. 1.

IV. Practical Considerations

For successful application of the proposed method to model WPT systems, the initial settings have to be properly specified. These include: 1) how to determine the polynomial degrees $\{n_j, m_j\}_{j=1}^{n_u}$, n_c and n_d; 2) how to select the initial parameters, since the proposed method is a bootstrap procedure; 3) how to determine the upper and lower boundaries of the time delays.

A. Choice of Polynomial Degrees

The choice of n_j and m_j requires the establishment of an equivalent circuit for the WPT system by regarding the switches and diodes as ideal ones: see Fig. 6, where R_j, $j = 0, 1, \ldots, n_u$, accounts for the equivalent series resistance of the jth resonator, and v_j, $j = 1, \ldots, n_u$, is an AC source to replace the phase-controlled full-bridge inverter of the jth transmitter. For the WPT system under consideration, there are two main operating modes:

1) If driving frequency of the system is exactly equal to the resonant frequency f_0, all resonators of the circuit become resistive, so that the output filtering capacitor C_f is the only reactive component in the circuit. In this sense, it is straightforward that the model of the system is of first order, i.e., $n_j = 1$, $m_j = 0$, $j = 1, \ldots, n_u$. The idea used for model order selection follows the concept of data-based mechanistic modeling introduced in [48], which aims at looking for the dominant physical mechanism that governs the system and, subsequently, investigates how this can be modeled in the simplest manner.
2) If driving frequency of the system is slightly larger than the resonant frequency f_0, the inductive behaviors of the resonators are not fully compensated for by the capacitor connected in series. In this situation, the resonant tank is inductive, and thus the whole circuit could be explained by a second-order model, i.e., $n_j = 2$, and $m_j = 0$ or 1, provided that the driving-resonant frequency mismatch is not very large. Note that a high-order model can have

[1]The TFRIVC method will be included in the CONTSID toolbox which can be downloaded from http://www.cran.univ-lorraine.fr/contsid/.

better explanatory abilities, but this is not very attractive, since low-order models are always preferred in control design if they provide a sufficiently accurate description of the system dynamics.

Practical WPT systems normally work at the second mode to protect the switching devices. Therefore, a simple plant model up to order two is always enough for dynamic modeling: see also [25]. A simpler way to help select the model order is to observe the waveform of the output response: if there is a clear oscillation in this response, a second-order model is suggested; otherwise, a first-order model is preferred. On the other hand, the choice of n_c and n_d can be achieved, as normal in time-series analysis, by reference to statistical measures, such as the coefficient of determination R_T^2 and model order identification criteria (see [28], [45]). One should be aware that the choice of n_c and n_d is not critical, since the proposed IV method is able to generate statistically consistent estimates, even if the noise model is not correctly specified (although their correct identification ensures lower variance estimates).

B. Choice of Initial Parameters

To initiate the proposed bootstrap estimation procedure, initial parameters $\{\boldsymbol{\theta}_j^*, \tau_j^*\}$ are required in order to compute the filtered signals in (17) and (18), as well as the gradient and Hessian in (24). To this end, two methods are suggested to generate $\{\boldsymbol{\theta}_j^*\}$ when the time delays are assumed to be known:

1) Circuit theory-based method. This method is preferred when the experimenter has an enough *a priori* information about the circuit topology and component parameters.
2) State variable filter-based IV (IVSVF) method. This is a more user-friendly data-driven method, requiring only a few initial settings, i.e., the cutoff frequency of the state variable filter λ, and the polynomial degrees $\{n_j, m_j\}_{j=1}^{n_u}$.

The interested reader is directed to [25] for further details on the first method, while the latter method is summarized in Algorithm 2. See [25] for a guideline regarding the choice of λ. On the other hand, selection of $\{\tau_j^*\}$ should be carried out with special care, since the cost function is always non-convex with respect to the time delays. As a consequence, the estimation procedure is possibly trapped by local minima if initial time delays are not suitably selected. In order to relieve this problem, it is suggested that a grid of initial time delay values is used. Then, we estimate a rational model at each grid point, using the IVSVF method with the time delays being fixed; subsequently, amongst the resulting models, the one that has the minimal cost is used as the initial model for the basic TFRIVC method. The above discussion leads to a more robust implementation of TFRIVC; see Algorithm 3.

C. Choice of Time-Delay Boundaries

The choice of time-delay boundaries in the SISO scenario has been discussed in our previous paper [25]. By default, one can simply let $\underline{\tau}_j = 0$ if no *a priori* knowledge is available; while the upper boundary can be computed based on sampled input–output data by minimizing the following cross-correlation function:

$$\overline{\tau}_j = \arg\max_{\tau_j} \left| \mathbb{E}\left\{ y_j(t_k) u_j(t_k - \tau_j) \right\} \right| \tag{33}$$

where $\mathbb{E}$ is the expectation operator. Note that the resulting $\overline{\tau}_j$ is always larger than the true time delay if the system is causal [25]. However, there is a difficulty in direct implementation of (33), due to the unknown $y_j(t_k)$ in the MISO scenario. To circumvent this problem, it is suggested $\{\boldsymbol{\theta}_j\}$ is estimated using the IVSVF method by setting the time delays to the lower boundaries and, subsequently, computing $y_j(t_k)$ using (18), based on the models obtained from sampled data.

Algorithm 2: The IVSVF method.

Input:
- Sampled data: $\{y(t_k), u_1(t_k), \ldots, u_{n_u}(t_k)\}_{k=1}^N$;
- Polynomial degrees: $\{n_j, m_j\}_{j=1}^{n_u}$;
- Cutoff frequency: λ;
- Initial time delays: $\{\tau_j^*\}_{j=1}^{n_u}$;

Output: $\{\boldsymbol{\theta}_j^*\}_{j=1}^{n_u}$;

for $j \leftarrow 1$ **to** n_u **do**
- $y_j(t_k) \leftarrow y(t_k)$;
- compute $\tilde{\boldsymbol{\phi}}_j^\top(t_k, \tau_j^*)$ in (16) and $\tilde{y}_j^{(n_j)}(t_k)$ in (17) using $F(p) = 1/(p+\lambda)^{n_j}$;
- generate $\boldsymbol{\theta}_j^*$ using the LS estimator

$$\boldsymbol{\theta}_j^* \leftarrow \left[\sum_{k=1}^N \tilde{\boldsymbol{\phi}}_j(t_k, \tau_j^*) \tilde{\boldsymbol{\phi}}_j^\top(t_k, \tau_j^*) \right]^{-1} \times \sum_{k=1}^N \tilde{\boldsymbol{\phi}}_j(t_k, \tau_j^*) \tilde{y}_j^{(n_j)}(t_k);$$

end

for $j \leftarrow 1$ **to** n_u **do**
- compute $y_j(t_k)$ in (18) using $\{\boldsymbol{\theta}_j^*, \tau_j^*\}_{j=1}^{n_u}$;
- compute $\tilde{\boldsymbol{\phi}}_j^\top(t_k, \tau_j^*)$ in (16), $\tilde{y}_j^{(n_j)}(t_k)$ in (17), and $\hat{\boldsymbol{\phi}}_j^\top(t_k)$ in (21) using $\boldsymbol{\theta}_j^*$ and τ_j^*;
- refine $\boldsymbol{\theta}_j^*$ using the IV estimator

$$\boldsymbol{\theta}_j^* \leftarrow \left[\sum_{k=1}^N \hat{\boldsymbol{\phi}}_j(t_k) \tilde{\boldsymbol{\phi}}_j^\top(t_k, \tau_j^*) \right]^{-1} \times \sum_{k=1}^N \hat{\boldsymbol{\phi}}_j(t_k) \tilde{y}_j^{(n_j)}(t_k);$$

end

V. Simulation Example

In this section, the effectiveness of the proposed method was illustrated by numerical simulation. The input–output data used for model estimation were generated by using Simulink in Matlab; see Fig. 4 for the circuit diagram. The system under consideration consisted of two phase-controlled full-bridge inverters and one receiver, with the main circuit component

Algorithm 3: The robust TFRIVC method.

Input:

- Sampled data: $\{y(t_k), u_1(t_k), \ldots, u_{n_u}(t_k)\}_{k=1}^{N}$;
- Polynomial degrees: $\{n_j, m_j\}_{j=1}^{n_u}$, n_c, n_d;
- Cutoff frequency: λ;
- Number of time delays to be compared: $\{K_j\}_{j=1}^{n_u}$;
- Maximum iteration number: $N_{\max}$;
- Tolerances of cost and parameter changes: ς_{fun}, ς_{par};
- Lower and upper time-delay boundaries: $\{\underline{\tau}_j, \overline{\tau}_j\}_{j=1}^{n_u}$;

Output: $\boldsymbol{\vartheta}^*$;

define $\boldsymbol{\vartheta} = \left[\boldsymbol{\theta}_1^\top, \tau_1, \ldots, \boldsymbol{\theta}_{n_u}^\top, \tau_{n_u}\right]^\top$;

define the set of possible time-delay combinations:

$$S = \big\{(\tau_1, \ldots, \tau_{n_u}) : \tau_j = \underline{\tau}_j + i(\overline{\tau}_j - \underline{\tau}_j)/K_j; \\ 0 \leqslant i \leqslant K_j; 1 \leqslant j \leqslant n_u\big\};$$

set initial time delays: $\{\hat{\tau}_j\}_{j=1}^{n_u} \leftarrow \{\underline{\tau}_j\}_{j=1}^{n_u}$;

apply the IVSVF algorithm to generate $\{\hat{\boldsymbol{\theta}}_j\}_{j=1}^{n_u}$;

foreach $(\tau_1, \ldots, \tau_{n_u}) \in S$ **do**

  for $j \leftarrow 1$ **to** n_u **do**

    compute $y_j(t_k)$ in (18) using $\{\hat{\boldsymbol{\theta}}_j, \hat{\tau}_j\}_{j=1}^{n_u}$;

  end

  for $j \leftarrow 1$ **to** n_u **do**

    $\hat{\tau}_j \leftarrow \tau_j$;

    compute $\tilde{\boldsymbol{\phi}}_j^\top(t_k, \hat{\tau}_j)$ in (16), $\tilde{y}_j^{(n_j)}(t_k)$ in (17), and $\hat{\boldsymbol{\phi}}_j^\top(t_k)$ in (21) using $\hat{\boldsymbol{\theta}}_j$ and $\hat{\tau}_j$;

    update $\hat{\boldsymbol{\theta}}_j$ using the IV estimator

$$\hat{\boldsymbol{\theta}}_j \leftarrow \left[\sum_{k=1}^{N} \hat{\boldsymbol{\phi}}_j(t_k)\tilde{\boldsymbol{\phi}}_j^\top(t_k, \hat{\tau}_j)\right]^{-1} \times \sum_{k=1}^{N} \hat{\boldsymbol{\phi}}_j(t_k)\tilde{y}_j^{(n_j)}(t_k);$$

  end

  compute $J(\hat{\boldsymbol{\vartheta}})$ in (11) with $H(q^{-1}, \boldsymbol{\eta}) = 1$;

end

$\boldsymbol{\vartheta}^* \leftarrow \arg\min_{\hat{\boldsymbol{\vartheta}}} J(\hat{\boldsymbol{\vartheta}})$;

compute $\hat{\xi}(t_k)$ in (32) using $\boldsymbol{\vartheta}^*$ and, based on which, generate $\boldsymbol{\eta}^*$ using an ARMA estimation routine;

$\boldsymbol{\vartheta}^* \leftarrow \left[(\boldsymbol{\vartheta}^*)^\top, (\boldsymbol{\eta}^*)^\top\right]^\top$;

apply the basic TFRIVC algorithm (see Algorithm 1) to refine $\boldsymbol{\vartheta}^*$;

parameters listed in Table I. The experiment was carried out in the following two steps:

1) Firstly, the inputs were initially set as: $u_1(t) = 0.8$, $u_2(t) = 0.7$, in order to establish a stationary working point. Here, the values stand for normalized phases, e.g., 0.8 corresponds to a actual phase angle of 144°. After the system had entered a steady state, the output voltage was measured to be 234.9 V.
2) Secondly, each input was perturbed by a test sequence to generate informative data for model identification. More specifically, $u_1(t)$ was perturbed by a pseudo-random binary sequence (PRBS) generated from an eight-stage shift register at a clock period $5T$, while $u_2(t)$ was perturbed by another PRBS generated from a seven-stage shift register at a clock period $10T$, where $T = 1$ ms is the sample time. Both PRBSs had the amplitude switching between ± 0.01.
3) Thirdly, as soon as the perturbations had been applied, the input–output signals were observed at time instant $t_k = kT$, $k = 1, 2, \ldots, 1280$. It was assumed that the input was noise-free, while the sampled output was corrupted by colored noise

$$y(t_k) = x(t_k) + \xi(t_k) \tag{34}$$

where $x(t_k)$ stands for the noise-free output, and $\xi(t_k)$ is a colored measurement noise that is a filtered version of white noise $e(t_k)$ through the following model:

$$\xi(t_k) = H(q^{-1}, \boldsymbol{\eta})e(t_k) = \frac{1 + 0.2497q^{-1}}{1 - 0.9744q^{-1} + 0.2231q^{-2}}e(t_k). \tag{35}$$

The variance of $e(t_k)$ was adjusted to achieve a signal-to-noise ratio (SNR) of 15 dB in the experiment, where SNR is defined as

$$\text{SNR} = 10\log_{10}\left(P_x/P_\xi\right) \text{ dB} \tag{36}$$

and P_x and P_ξ are the power of $x(t_k)$ and $\xi(t_k)$, respectively. See Fig. 5 for a portion of sampled data.

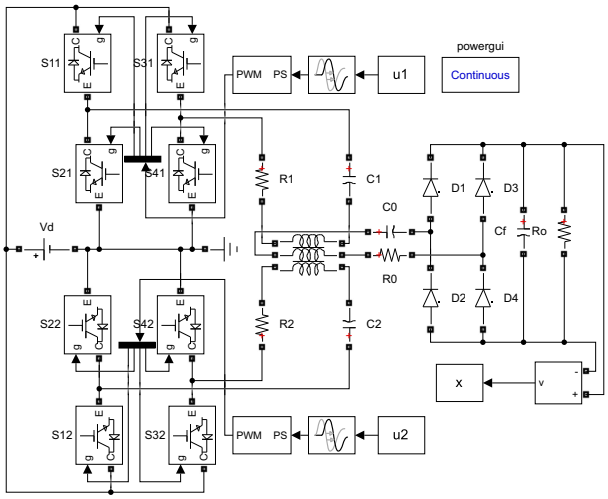

Fig. 4. Simulink diagram used for simulation study.

Note that the model estimated by the proposed method is, in fact, a small-signal model, so that the stationary values should be removed from the data before they are used for model estimation: i.e., $z(t_k) \leftarrow z(t_k) - \mathbb{E}\{z(t_k)\}$, where $z = y, u_1$ or u_2. However, these stationary values should be retained when plotting the responses of the estimated models, see later Figs. 6, 7, 10, and 11. According to the guidelines suggested in Section IV, the initial settings for the robust TFRIVC method were chosen as: $n_{a,1} = n_{a,2} = 2$; $n_{b,1} = n_{b,2} = 0$; $n_c = 2$; $n_d = 1$; $\underline{\tau}_1 = \underline{\tau}_2 = 0$ s; $\overline{\tau}_1 = 8$ ms; $\overline{\tau}_2 = 5$ ms; $\lambda = 1000$ rad/s; $K_1 = K_2 = 10$. The other parameters remained at their default values.

TABLE I
MAIN PARAMETERS OF THE SIMULINK DIAGRAM IN FIG. 4

Parameter	Explanation	Value
C_0	Capacitance of the receiver resonator	40 nF
C_1	Capacitance of the 1st transmitter resonator	40 nF
C_2	Capacitance of the 2nd transmitter resonator	40 nF
C_f	Capacitance of the output filter	2200 μF
f_s	Driving frequency of the inverters	80 kHz
L_0	Inductance of the receiver resonator	104 μH
L_1	Inductance of the 1st transmitter resonator	104 μH
L_2	Inductance of the 2nd transmitter resonator	104 μH
M_{10}	Mutual inductance between L_1 and L_0	1.83 μH
M_{20}	Mutual inductance between L_2 and L_0	5.50 μH
M_{21}	Mutual inductance between L_2 and L_1	-0.1 μH
R_0	Equivalent resistance of the L_0, C_0 branch	0.039 Ω
R_1	Equivalent resistance of the L_1, C_1 branch	0.039 Ω
R_2	Equivalent resistance of the L_2, C_2 branch	0.039 Ω
R_o	Load resistance	5 Ω
R_s	On-state resistance of the switches	0.001 Ω
τ_1	Delay of the 1st transmitter	4.5 ms
τ_2	Delay of the 2nd transmitter	1.5 ms
V_d	Voltage of the DC source	400 V
V_r	Forward voltage of the diodes	0.8 V

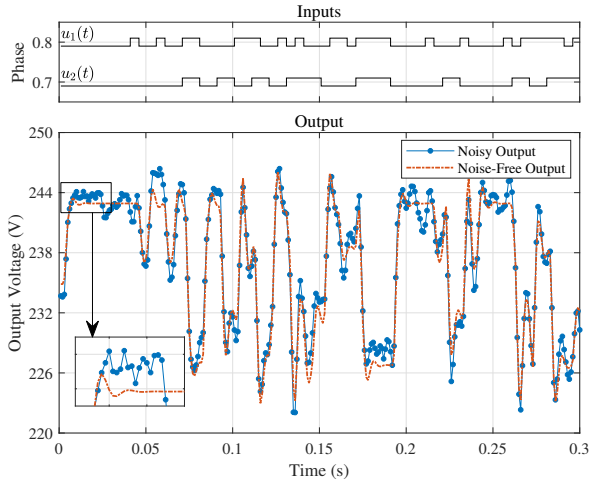

Fig. 5. Portion of the sampled input and output signals.

Remark 1: An interesting phenomenon, shown in the magnified part of Fig. 5, is that the system output has a clear oscillation when a step change is added to the input. This phenomenon can be explained by point 2 of Section IV-A: as the resonant frequency is $f_0 = 1/(2\pi\sqrt{L_0C_0}) = 78$ kHz, the resonant tank is inductive at the driving frequency $f_s = 80$ kHz, so that the whole circuit may behave as an LCR oscillator, whose output response shows an oscillatory component. This is why a second-order model has been adopted to represent the system.

The proposed robust TFRIVC method is called by the following statement:

```
[G,H]
 = tfrivc(data,[n_{a,1},n_{a,2}],[n_{b,1},n_{b,2}],...
   'tdmin',[τ_1,τ_2],'tdmax',[τ̄_1,τ̄_2],...
   'numtd',[K_1,K_2],'lambda',λ,...
   'nn',[n_c,n_d])
```

where `G` and `H` denote the resulting plant and noise models, respectively, and `data` is an `iddata` object from the Matlab system identification toolbox that contains the sampled input–output data. In a single run experiment, the estimated second-order model is

$$x(t) = \frac{-2.055 \times 10^8}{p^2 + 685.3p + 9.042 \times 10^5} u_1(t - 0.00454) + \frac{-5.103 \times 10^8}{p^2 + 698.1p + 8.769 \times 10^5} u_2(t - 0.00153) \quad (37)$$

$$\xi(t_k) = \frac{1 + 0.2459q^{-1}}{1 - 0.9908q^{-1} + 0.2626q^{-2}} e(t_k). \quad (38)$$

The accuracy of the above estimated model was evaluated by the performance index

$$\text{fit} = \left(1 - \frac{\|y(t_k) - y_s(t_k)\|_2}{\|y(t_k) - y_m(t_k)\|_2}\right) \times 100\% \quad (39)$$

where $y(t_k)$ is the sampled output, $y_s(t_k)$ is the simulated output generated from the estimated plant model, and $y_m(t_k)$ is the mean value of $y(t_k)$. The model response and the fit were computed using the `compare` routine from the Matlab system identification toolbox.

For comparative purposes, we also present the estimated first-order model

$$x(t) = \frac{-1.592 \times 10^5}{p + 559.8} u_1(t - 0.00489) + \frac{-1.622 \times 10^6}{p + 2761} u_2(t - 0.00281) \quad (40)$$

$$\xi(t_k) = \frac{1 - 0.0648q^{-1}}{1 - 1.201q^{-1} + 0.4783q^{-2}} e(t_k) \quad (41)$$

and the estimated third-order model

$$x(t) = \frac{-1.877 \times 10^4 p^2 - 2.117 \times 10^8 p + 6.004 \times 10^8}{p^3 + 705.2p^2 + 9.265 \times 10^5 p + 5.862 \times 10^5} \times u_1(t - 0.00466) + \frac{-476.3p^2 - 5.174 \times 10^8 p - 2.09 \times 10^9}{p^3 + 708.9p^2 + 8.904 \times 10^5 p + 2.361 \times 10^6} \times u_2(t - 0.00154) \quad (42)$$

$$\xi(t_k) = \frac{1 + 0.2406q^{-1}}{1 - 0.9915q^{-1} + 0.2687q^{-2}} e(t_k). \quad (43)$$

The fit ratios of the above three models in (37), (40), and (42) are listed in Table II, showing that the second-order model is more accurate than the first-order model; and it has almost the same accuracy as the third-order model. The responses of the estimated first- and second-order models when $u_1(t)$ steps from 0.8 to 0.79, and when $u_2(t)$ steps from 0.7 to

TABLE II
FIT RATIOS FOR THE ESTIMATED MODELS (37), (40), AND (42)

Model	Fit to noisy data	Fit to noise-free data
1st-order model (40)	71.59%	77.10%
2nd-order model (37)	82.50%	98.21%
3rd-order model (42)	82.73%	96.93%

TABLE III
ESTIMATED MODEL PARAMETERS

Method	Estimated Parameters Value (mean(±std))								$\overline{\text{fit}}$
	$\hat{a}_{1,1}$	$\hat{a}_{2,1}$	$\hat{b}_{0,1}$	$\hat{\tau}_1$	$\hat{a}_{1,2}$	$\hat{a}_{2,2}$	$\hat{b}_{0,2}$	$\hat{\tau}_2$	
SRIVC	651.9 (±42.0)	6.318×10^5 ($\pm 1.71 \times 10^4$)	-1.468×10^8 ($\pm 7.6 \times 10^6$)	0.004 (±0)	820.7 (±24.8)	1.264×10^6 ($\pm 2.3 \times 10^4$)	-7.325×10^8 ($\pm 1.80 \times 10^7$)	0.002 (±0)	80.40% (±0.35%)
TFRIVC	698.3 (±35.3)	8.796×10^5 ($\pm 2.72 \times 10^4$)	-2.014×10^8 ($\pm 8.6 \times 10^6$)	0.004513 ($\pm 3.5 \times 10^{-5}$)	698.8 (±17.9)	8.769×10^5 ($\pm 1.59 \times 10^4$)	-5.095×10^8 ($\pm 9.9 \times 10^6$)	0.001525 ($\pm 2 \times 10^{-5}$)	82.49% (±0.20%)

$\overline{\text{fit}}$–Mean fit value.

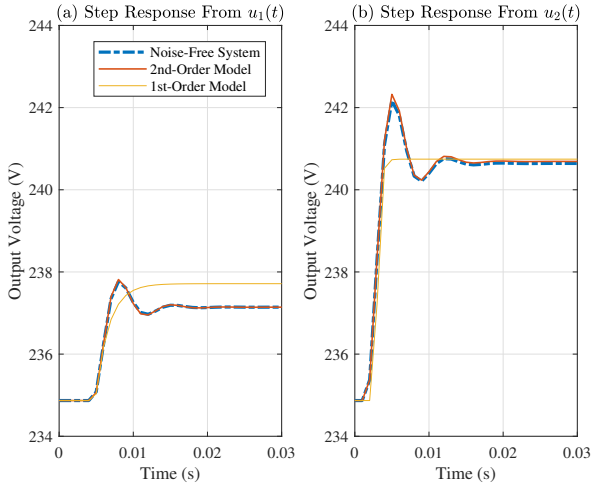

Fig. 6. Responses of the estimated first- and second-order models, when $u_1(t)$ steps from 0.8 to 0.79, and when $u_2(t)$ steps from 0.7 to 0.69.

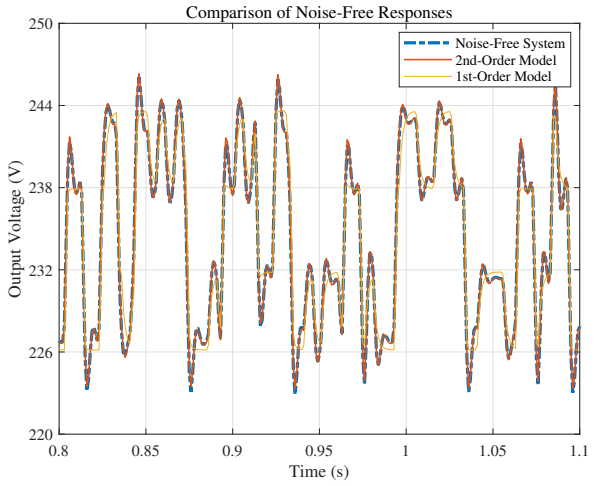

Fig. 7. Comparison of the noise-free responses of the estimated first- and second-order models.

0.69, are compared in Fig. 6. The noise-free outputs of the estimated first- and second-order models to the sampled inputs are compared in Fig. 7. Both figures confirm the accuracy of the estimated second-order model.

Subsequently, a Monte–Carlo (MC) simulation of 100 independent runs was conducted to show the statistical properties of the parameter estimates. To avoid standing alone, the SRIVC routine available from the CONTSID toolbox was implemented to show the improvement of the proposed fractional time-delay estimation method. SRIVC can be called in the following way to estimate a first-order, two-input, single-output model with known time delays:

`mp = srivc(data,[`$n_{b,1}$`,`$n_{b,2}$`,`$n_{a,1}$`,`$n_{a,2}$`,`$n_{k,1}$`,`$n_{k,2}$`]);`

where $n_{k,j}$, $j = 1$ or 2, constrained to be an integer number of the sample time, is the time delay of the jth input channel. By trial and error, it was found that the optimal values were $n_{k,1} = 4$ and $n_{k,2} = 2$ for this example.

For each MC run, the WPT system was initially in a stationary state, so the initial model state was set to zero during the model estimation process. The parameter estimates generated by the SRIVC and TFRIVC methods from the 100 MC runs are listed in Table III, from which it is clear that SRIVC performs quite well here because good integer time delays have been given to the algorithm; while TFRIVC improves the fit ratio by 2.09% compared with SRIVC, thanks to its capability of estimating fractional time delays. Note that the estimated noise model parameters by TFRIVC are not shown in this table, due to the space constraints.

VI. EXPERIMENTAL EXAMPLE

In this section, the effectiveness of the proposed method was evaluated using real data generated by the experimental apparatus shown in Fig. 8, where two phase-controlled full-bridge inverters were used to power a single receiver. The measurement and control was implemented on a National Instruments (NI) CompactRIO system, which had two built-in controllers: a 1.33-GHz Intel Atom CPU, and a Kintex-7 70T field-programmable gate array (FPGA). The full-bridge inverters were composed of four TI CSD19534 N-channel MOSFETs, whose typical drain-to-source voltage and drain current were 100 V and 10 A, respectively. The pulse width modulation (PWM) signals to drive these MOSFETs were generated by the interval FPGA of CompactRIO, and exported by an NI-9401, which was a 5 V/TTL, 8 bidirectional channel, 100-ns digital module. The output voltage was measured by the CPU via an NI-9201, which was a ±10 V, 500 kS/s, 12-bit, 8-channel voltage input module. The three resonators had the same design parameters: all coils were round and made by Litz wire of 1200 strands, each strand having a diameter of 0.01 mm, in order to relieve the skin effect. Moreover, the number of coil turns was 21, with the outer and inner diameters

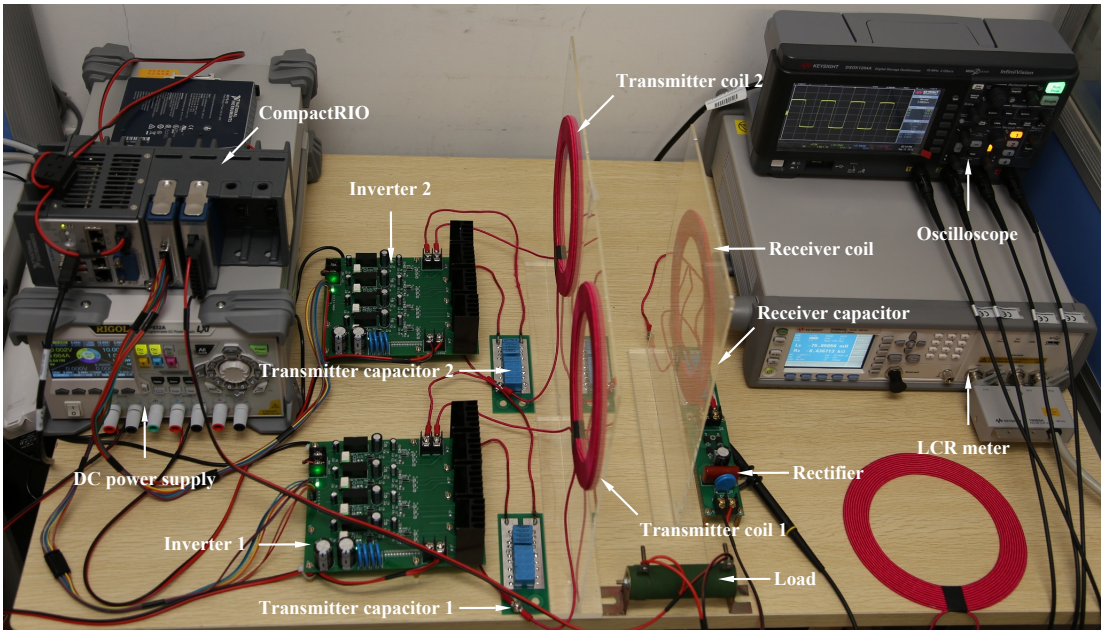

Fig. 8. Experimental apparatus.

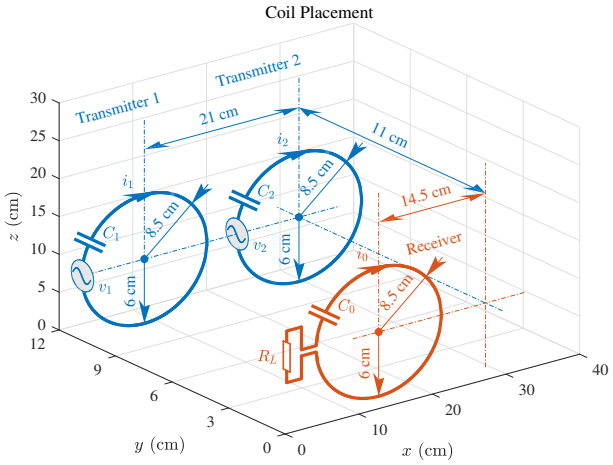

Fig. 9. Coil placement, where R_L is the equivalent impedance to replace the rectifier and load.

TABLE IV
MAIN PARAMETERS OF THE EXPERIMENTAL APPARATUS

Parameter	Explanation	Value
C_0	Capacitance of the receiver resonator	37.76 nF
C_1	Capacitance of the 1st transmitter resonator	38.59 nF
C_2	Capacitance of the 2nd transmitter resonator	38.06 nF
C_f	Capacitance of the output filter	471.2 μF
f_s	Driving frequency of the inverters	80 kHz
L_0	Inductance of the receiver resonator	104.3 μH
L_1	Inductance of the 1st transmitter resonator	104.4 μH
L_2	Inductance of the 2nd transmitter resonator	105.2 μH
M_{10}	Mutual inductance between L_1 and L_0	4.234 μH
M_{20}	Mutual inductance between L_2 and L_0	2.224 μH
M_{21}	Mutual inductance between L_2 and L_1	-1.823 μH
R_0	Equivalent resistance of the L_0, C_0 branch	162.4 mΩ
R_1	Equivalent resistance of the L_1, C_1 branch	161.1 mΩ
R_2	Equivalent resistance of the L_2, C_2 branch	162.0 mΩ
R_o	Load resistance	9.7 Ω
R_s	On-state resistance of the switches	12.6 mΩ
V_d	Voltage of the DC source	7 V
V_r	Forward voltage of the diodes	0.5 V

of 17 and 12 cm, respectively. The vertical distances between the transmitter and receiver coil planes were 11 cm: see Fig. 9 for more details about the coil placement. Each capacitor bank to compensate for the leakage inductance was made of five 6.8-nF film capacitors and four 1-nF film capacitors. To convert the high-frequency AC voltage at the receiver side to DC voltage, a rectifier consisting of four SS34 Schottky diodes was used, together with three types of capacitors to further smooth the output voltage: an electrolytic capacitor of 470 μF, a polypropylene capacitor of 1 μF, and two ceramic capacitors of 100 nF. However, due to the manufacturing errors, the coils or compensating capacitors cannot be identical. Therefore, their parameter values were measured by a Keysight E4980AL LCR meter at 80 kHz; see Table IV. Since the on-board clock of the FPGA was 40 MHz, each PWM period was configured to cover 500 clock periods, so that an 80-kHz driving frequency was obtained. In this situation, the resolution of the normalized phase shift was $1/250 = 0.004$.

To generate experimental data for model identification, we followed the same procedure presented in Section V:

1) Firstly, to set up a stationary working point, let $u_1(t) = 0.7$ and $u_2(t) = 0.8$ and, then, the stationary output was measured to be $y(t) = 7.443$ V. At this state, the input power of the first transmitter was 7.074 W, while the power of the second transmitter was 5.492 W, measured by a Rigol DP832A programmable DC power supply. Given a 9.7-Ω resistive load, the overall efficiency of the prototype was $7.443^2/9.7/(7.074 + 5.472) \times 100\% = 45.52\%$. This was a quite low efficiency, due to the

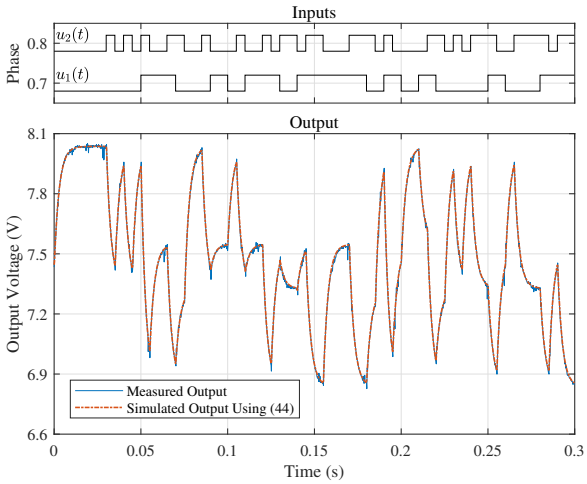

Fig. 10. Portion of experimental data, together with the simulated output using the first-order model (44).

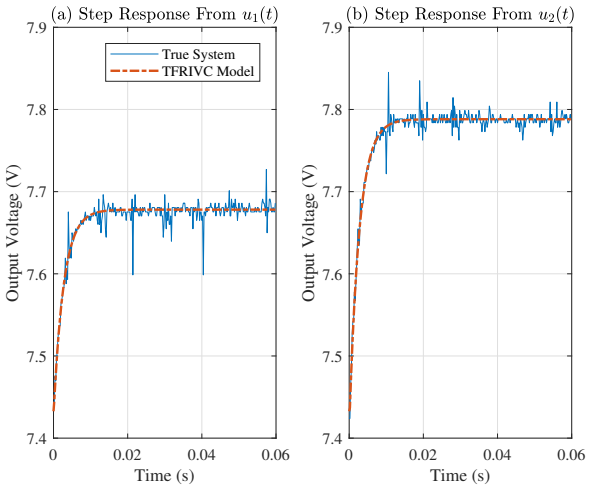

Fig. 11. Responses of the true system and estimated models, when $u_1(t)$ steps from 0.7 to 0.68, and when $u_2(t)$ steps from 0.8 to 0.78.

significant misalignment between the transmitter and receiver coils. However, the experiments has shown that the power efficiency in the single transmitter case can reach up to 85% if perfect alignment is ensured.

2) Secondly, the two inputs were simultaneously perturbed by PRBSs to persistently excite the system. In particular, $u_1(t)$ was perturbed by a PRBS generated from a five-stage shift register at a clock period $50T$, where $T = 0.2$ ms is the sample time, while $u_2(t)$ was perturbed by a PRBS generated from a six-stage shift register at a clock period $25T$. Both PRBSs had their amplitude switching between ± 0.02.

3) Lastly, when the test sequences had been applied, the input–output signals were observed at sampling instant $t_k = kT, k = 1, \ldots, 1600$. The sampled input–output data are denoted as $\{y(t_k), u_1(t_k), u_2(t_k)\}_{k=1}^{1600}$; see Fig. 10 for a portion of observed input–output data.

As shown in Fig. 10, the output response does not have any oscillatory component, even if the inputs have numerous sharp changes, suggesting that a first-order model should explain the input–output behavior of the system, according to the guidelines presented in Section IV-A. To confirm this initial conjecture, first- and second-order models were estimated using the experimental data shown in Fig. 10. The estimated first-order model is then

$$x(t) = \frac{-4501}{p + 368.2} u_1(t - 6.72 \times 10^{-5}) + \frac{-6644}{p + 374.8} u_2(t - 0.000161) \quad (44)$$

with a fit ratio being 96.49%: see Fig. 10 for a comparison between the measured output and the simulated output of this model. The estimated second-order model is

$$x(t) = \frac{-9.76 \times 10^7}{p^2 + 2.21 \times 10^4 p + 7.982 \times 10^6} u_1(t - 1.48 \times 10^{-5}) + \frac{-2.347 \times 10^8}{p^2 + 3.576 \times 10^4 p + 1.323 \times 10^7} u_2(t - 0.000127) \quad (45)$$

TABLE V
ESTIMATED MODEL PARAMETERS

Parameter	Value (mean($\pm$std))
$\hat{a}_{1,1}$	366.2($\pm$1.9)
$\hat{b}_{0,1}$	$-4493(\pm 21)$
$\hat{\tau}_1$	$6.691 \times 10^{-5}(\pm 9.75 \times 10^{-6})$
$\hat{a}_{1,2}$	373.0($\pm$1.5)
$\hat{b}_{0,2}$	$-6628(\pm 22)$
$\hat{\tau}_2$	$0.0001673(\pm 3 \times 10^{-5})$
$\overline{\text{fit}}$	96.10%($\pm$0.15%)
$\overline{N}_{\text{iter}}$	6.0
$\overline{T}_{\text{c}}$	0.27 s

$\overline{\text{fit}}$–Mean fit value.
$\overline{N}_{\text{iter}}$–Mean iteration number.
$\overline{T}_{\text{c}}$–Mean computing time.

with a fit ratio being 96.49%. Comparison of the two fit ratios shows that both models explain the data very well, so that a first-order model is, indeed, sufficient to provide a satisfactory explanation of the experimental data. Note that the noise model was not estimated since, as shown in Fig. 10, the measurement noise level is quite low and so has a negligible impact on the estimated parameters.

Subsequently, 100 independent experiments were carried out to investigate the statistical properties of the parameter estimates. For each experiment, the WPT system was initially in a stationary state, so the initial model state was set to zero in the application of the TFRIVC method. The initial settings were chosen as: $n_{a,1} = n_{a,2} = 1$; $n_{b,1} = n_{b,2} = 0$; $\underline{\tau}_1 = \underline{\tau}_2 = 0$ s; $\overline{\tau}_1 = 2.8$ ms; $\overline{\tau}_1 = 2.2$ ms; $\lambda = 100$ rad/s; $K_1 = K_2 = 5$. The parameter estimates generated from the 100 experiments are listed in Table V, showing a very high fit ratio ($\overline{\text{fit}} = 96.1\%$) and a fast convergence rate $\overline{T}_c = 0.27$ s. It is also interesting to observe that the estimated time delays are quite small, only one or two sample times, because the output voltage is sampled by CompactRIO directly. Note that practical WPT systems are seldom in this case, where sampling of the output voltage is usually done by a remote sensor, with data transferred to the

host computed via wireless communication, which inevitably introduces longer time delays.

Finally, we computed the responses of the estimated model, constructed by using the mean parameter values given in Table V, when $u_1(t)$ steps from 0.7 to 0.68, and when $u_2(t)$ steps from 0.8 to 0.78; see Fig. 11 for the comparison results, where the step responses of the true system are also plotted. These results confirm again the accuracy and effectiveness of the proposed method.

VII. Conclusions

In this paper, a new method was developed for the data-driven modeling of MISO WPT systems where, in addition to the process parameters, pure time delays and colored measurement noise can be estimated simultaneously. In contrast to conventional circuit theory-based modeling methods that require full information on the circuit, the proposed method is very user-friendly, requiring only sampled input–output data and a few initial settings that can be selected easily according to the suggested guidelines. Most importantly, the proposed method yields simple low-order models plus time delays that are of a form that is well suited for control system design. Simulation results have shown that the MISO WPT system can be satisfactorily described by a second-order model if the system is under-damped; and that the proposed method generates a very accurate second-order model, even when there is a reasonable level of noise on the sampled data. Experimental results have shown that over-damped systems can be modeled by a first-order model and, for the prototype used in the real-data experiment, the proposed method yielded a high fit ratio of up to 96% in this first-order modeling scenario.

References

[1] A. Kurs, A. Karalis, R. Moffatt, J. D. Joannopoulos, P. Fisher, and M. Soljačić, "Wireless power transfer via strongly coupled magnetic resonances," *Science*, vol. 317, no. 83, pp. 83–86, 2007.

[2] S. Y. R. Hui, W. Zhong, and C. K. Lee, "A critical review of recent progress in mid-range wireless power transfer," *IEEE Transactions on Power Electronics*, vol. 29, no. 9, pp. 4500–4511, September 2014.

[3] S. Y. R. Hui and W. W. Ho, "A new generation of universal contactless battery charging platform for portable consumer electronic equipment," *IEEE Transactions on Power Electronics*, vol. 20, no. 3, pp. 620–627, May 2005.

[4] B. Kallel, O. Kanoun, and H. Trabelsi, "Large air gap misalignment tolerable multi-coil inductive power transfer for wireless sensors," *IET Power Electronics*, vol. 9, no. 8, pp. 1768–1774, June 2016.

[5] P. Si, A. P. Hu, S. Malpas, and D. Budgett, "A frequency control method for regulating wireless power to implantable devices," *IEEE Transactions on Biomedical Circuits and Systems*, vol. 2, no. 1, pp. 22–29, March 2008.

[6] H. Liu, Q. Shao, and X. Fang, "Modeling and optimization of class-E amplifier at subnominal condition in a wireless power transfer system for biomedical implants," *IEEE Transactions on Biomedical Circuits and Systems*, vol. 11, no. 1, pp. 35–43, February 2017.

[7] G. A. Covic, J. T. Boys, M. L. Kissin, and H. G. Lu, "A three-phase inductive power transfer system for roadway-powered vehicles," *IEEE Transactions on Industrial Electronics*, vol. 54, no. 6, pp. 3370–3378, December 2007.

[8] F. Musavi and W. Eberle, "Overview of wireless power transfer technologies for electric vehicle battery charging," *IET Power Electronics*, vol. 7, no. 1, pp. 60–66, January 2014.

[9] X. Dai, J. C. Jiang, and J. Q. Wu, "Charging area determining and power enhancement method for multiexcitation unit configuration of wirelessly dynamic charging EV system," *IEEE Transactions on Industrial Electronics*, vol. 66, no. 5, pp. 4086–4096, May 2019.

[10] I. J. Yoon and H. Ling, "Investigation of near-field wireless power transfer under multiple transmitters," *IEEE Antennas and Wireless Propagation Letters*, vol. 10, pp. 662–665, 2011.

[11] D. Ahn and S. Hong, "Effect of coupling between multiple transmitters or multiple receivers on wireless power transfer," *IEEE Transactions on Industrial Electronics*, vol. 60, no. 7, pp. 2602–2613, July 2013.

[12] R. Johari, J. V. Krogmeier, and D. J. Love, "Analysis and practical considerations in implementing multiple transmitters for wireless power transfer via coupled magnetic resonance," *IEEE Transactions on Industrial Electronics*, vol. 61, no. 4, pp. 1774–1783, April 2014.

[13] H. D. Lang and C. D. Sarris, "Semidefinite relaxation-based optimization of multiple-input wireless power transfer systems," *IEEE Transactions on Microwave Theory and Techniques*, vol. 65, no. 11, pp. 4294–4306, November 2017.

[14] Y. Li, R. Mai, L. Lu, T. Lin, Y. Liu, and Z. He, "Analysis and transmitter currents decomposition based control for multiple overlapped transmitters based WPT systems considering cross couplings," *IEEE Transactions on Power Electronics*, vol. 33, no. 2, pp. 1829–1842, February 2018.

[15] S. Huh and D. Ahn, "Two-transmitter wireless power transfer with optimal activation and current selection of transmitters," *IEEE Transactions on Power Electronics*, vol. 33, no. 6, pp. 4957–4967, June 2018.

[16] D. Czarkowski and M. K. Kazimierczuk, "Energy-conservation approach to modeling PWM DC-DC converters," *IEEE Transactions on Aerospace and Electronic Systems*, vol. AES-29, no. 3, pp. 1059–1063, July 1993.

[17] S. Zheng and D. Czarkowski, "Modeling and digital control of a phase-controlled series–parallel resonant converter," *IEEE Transactions on Industrial Electronics*, vol. 54, no. 2, pp. 707–715, April 2007.

[18] Z. U. Zahid, Z. M. Dalala, C. Zheng, R. Chen, W. E. Faraci, J. S. Lai, G. Lisi, and D. Anderson, "Modeling and control of series–series compensated inductive power transfer system," *IEEE Journal of Emerging and Selected Topics in Power Electronics*, vol. 3, no. 1, pp. 111–123, March 2015.

[19] H. Hao, G. A. Covic, and J. T. Boys, "An approximate dynamic model of LCL-T-based inductive power transfer power supplies," *IEEE Transactions on Power Electronics*, vol. 29, no. 10, pp. 5554–5567, October 2014.

[20] S. Li and C. T. Mi, "Wireless power transfer for electric vehicle applications," *IEEE Journal of Emerging and Selected Topics in Power Electronics*, vol. 3, no. 1, pp. 4–17, March 2015.

[21] A. Ayachit and M. K. Kazimierczuk, "Transfer functions of a transformer at different values of coupling coefficient," *IET Circuits, Devices and Systems*, vol. 10, no. 4, pp. 337–348, July 2016.

[22] J. Tang, S. Dong, C. Cui, and Q. Zhang, "Sampled-data modeling for wireless power transfer systems," *IEEE Transactions on Power Electronics*, to be published. DOI 10.1109/TPEL.2019.2928739.

[23] S. Samanta and A. K. Rathore, "Small-signal modeling and closed-loop control of a parallel–series/series resonant converter for wireless inductive power transfer," *IEEE Transactions on Industrial Electronics*, vol. 66, no. 1, pp. 172–182, January 2019.

[24] Q. Deng, Z. Wang, C. Chen, D. Czarkowski, M. K. Kazimierczuk, H. Zhou, and W. Hu, "Modeling and control of inductive power transfer system supplied by multiphase phase-controlled inverter," *IEEE Transactions on Power Electronics*, vol. 34, no. 9, pp. 9303–9315, September 2019.

[25] F. Chen, H. Garnier, Q. Deng, M. K. Kazimierczuk, and X. Zhuan, "Control-oriented modeling of wireless power transfer systems with phase-shift control," *IEEE Transactions on Power Electronics*, to be published. DOI 10.1109/TPEL.2019.2920863.

[26] L. Ljung, *System Identification—Theory for the User*. Upper Saddle River: Prentice-Hall, 1999.

[27] H. Garnier and L. Wang (Eds.), *Identification of Continuous-time Models from Sampled Data*. London: Springer-Verlag, 2008.

[28] P. C. Young, *Recursive Estimation and Time-series Analysis: An Introduction for the Student and Practitioner*. Berlin: Springer-Verlag, 2011.

[29] T. T. Vu, S. O'Driscoll, and J. V. Ringwood, "Nonlinear dynamic transformer time-domain identification for power converter applications," *IEEE Transactions on Power Electronics*, vol. 29, no. 1, pp. 318–327, January 2014.

[30] V. Valdivia, A. Barrado, A. Lázaro, P. Zumel, C. Raga, and C. Fernández, "Simple modeling and identification procedures for "black-box" behavioral modeling of power converters based on transient response analysis," *IEEE Transactions on Power Electronics*, vol. 24, no. 12, pp. 2776–2790, December 2009.

[31] M. Ahmeid, M. Armstrong, S. Gadoue, M. Al-Greer, and P. Missailidis, "Real-time parameter estimation of DC–DC converters using a self-tuned kalman filter," *IEEE Transactions on Power Electronics*, vol. 32, no. 7, pp. 5666–5674, July 2017.
[32] M. Al-Greer, M. Armstrong, M. Ahmeid, and D. Giaouris, "Advances on system identification techniques for DC–DC switch mode power converter applications," *IEEE Transactions on Power Electronics*, vol. 34, no. 7, pp. 6973–6990, July 2019.
[33] F. Chen, X. Zhuan, H. Garnier, and M. Gilson, "Issues in separable identification of continuous-time models with time-delay," *Automatica*, vol. 94, pp. 258–273, 2018.
[34] A. Ayachit, F. Corti, A. Reatti, and M. K. Kazimierczuk, "Zero-voltage switching operation of transformer class-E inverter at any coupling coefficient," *IEEE Transactions on Industrial Electronics*, vol. 66, no. 3, pp. 1809–1819, March 2019.
[35] M. K. Kazimierczuk and D. Czarkowski, *Resonant Power Converters*. New York, NY: IEEE Press and John Wiley & Sons, 2011.
[36] M. K. Kazimierczuk, "Synthesis of phase-modulated resonant DC/AC inverters and DC/DC convertors," *IEE Proceedings B (Electric Power Applications)*, vol. 139, no. 4, pp. 387–394, July 1992.
[37] D. Czarkowski and M. K. Kazimierczuk, "Phase-controlled CLL resonant converter," in *Proceedings of the IEEE Applied Power Electronics Conference*, San Diego, CA, March 7–11 1993, pp. 432–438.
[38] N. Kollipara, M. K. Kazimierczuk, A. Reatti, and F. Corti, "Phase-control and power optimization of LLC converter," in *IEEE International Symposium on Circuits and Systems (ISCAS'2019)*, Sapporo, Japan, May 26–29 2019.
[39] P. C. Young, H. Garnier, and M. Gilson, "Refined instrumental variable identification of continuous-time hybrid Box–Jenkins models," in *Identification of Continuous-time Models from Sampled Data (H. Garnier and L. Wang (Eds.))*. London: Springer-Verlag, 2008, pp. 91–132.
[40] P. C. Young, "Refined instrumental variable estimation: Maximum likelihood optimization of a unified Box–Jenkins model," *Automatica*, vol. 51, no. 1, pp. 35–46, 2015.
[41] P. C. Young and H. Garnier, "Identification and estimation of continuous-time data-based mechanistic (DBM) models for environmental systems," *Environmental Modelling and Software*, vol. 21, no. 8, pp. 1055–1072, 2006.
[42] H. Garnier and P. C. Young, "The advantages of directly identifying continuous-time transfer function models in practical applications," *International Journal of Control*, vol. 87, no. 7, pp. 1319–1338, 2014.
[43] H. Garnier, "Direct continuous-time approaches to system identification. Overview and benefits for practical applications," *European Journal of Control*, vol. 24, pp. 50–62, 2015.
[44] F. Chen, H. Garnier, A. Padilla, and M. Gilson, "Recursive IV identification of continuous-time models with time delay from sampled data," *IEEE Transactions on Control Systems Technology*, to be published. DOI 10.1109/TCST.2019.2896124.
[45] H. Garnier, M. Gilson, P. C. Young, and E. Huselstein, "An optimal IV technique for identifying continuous-time transfer function model of multiple input systems," *Control Engineering Practice*, vol. 15, no. 4, pp. 471–486, 2007.
[46] A. J. Jakeman, L. P. Steele, and P. C. Young, "Instrumental variable algorithms for multiple input systems described by multiple transfer functions," *IEEE Transactions on Systems, Man, and Cybernetics*, vol. SMC-10, pp. 593–602, October 1980.
[47] F. Chen, H. Garnier, and M. Gilson, "Robust identification of continuous-time models with arbitrary time-delay from irregularly sampled data," *Journal of Process Control*, vol. 25, pp. 19–27, 2015.
[48] P. C. Young, "Data-based mechanistic modelling and forecasting globally averaged surface temperature," *International Journal of Forecasting*, vol. 34, no. 2, pp. 314–335, 2018.